



This is a repository copy of *Vascular patterning of subcutaneous mouse fibrosarcomas expressing individual VEGF isoforms can be differentiated using angiographic optical coherence tomography*.

White Rose Research Online URL for this paper:

<http://eprints.whiterose.ac.uk/123369/>

Version: Accepted Version

Article:

Byers, R.A., Fisher, M., Brown, N.J. orcid.org/0000-0002-2100-1905 et al. (2 more authors) (2017) Vascular patterning of subcutaneous mouse fibrosarcomas expressing individual VEGF isoforms can be differentiated using angiographic optical coherence tomography. *Biomedical Optics Express*, 8 (10). pp. 4551-4567. ISSN 2156-7085

<https://doi.org/10.1364/BOE.8.004551>

Reuse

Unless indicated otherwise, fulltext items are protected by copyright with all rights reserved. The copyright exception in section 29 of the Copyright, Designs and Patents Act 1988 allows the making of a single copy solely for the purpose of non-commercial research or private study within the limits of fair dealing. The publisher or other rights-holder may allow further reproduction and re-use of this version - refer to the White Rose Research Online record for this item. Where records identify the publisher as the copyright holder, users can verify any specific terms of use on the publisher's website.

Takedown

If you consider content in White Rose Research Online to be in breach of UK law, please notify us by emailing eprints@whiterose.ac.uk including the URL of the record and the reason for the withdrawal request.

Vascular patterning of subcutaneous mouse fibrosarcomas expressing individual VEGF isoforms can be differentiated using angiographic optical coherence tomography.

ROBERT A. BYERS,^{1,*} MATTHEW FISHER,² NICOLA J. BROWN,²
GILLIAN M. TOZER,^{2,†} AND STEPHEN J. MATCHER^{1,†}

¹ Biophotonics Group, Kroto Research Institute, University of Sheffield, Sheffield, UK

² Department of Oncology & Metabolism, The Medical School, University of Sheffield, Sheffield, UK

[†]GT and SM are Joint Senior Authors

rabyers1@sheffield.ac.uk

Abstract: Subcutaneously implanted experimental tumors in mice are commonly used in cancer research. Despite their superficial location, they remain a challenge to image non-invasively at sufficient spatial resolution for microvascular studies. Here we evaluate the capabilities of optical coherence tomography (OCT) angiography for imaging such tumors directly through the murine skin in-vivo. Datasets were collected from mouse tumors derived from fibrosarcoma cells genetically engineered to express only single splice variant isoforms of vascular endothelial growth factor A (VEGF); either VEGF120 or VEGF188 (fs120 and fs188 tumors respectively). Measured vessel diameter was found to be significantly ($p<0.001$) higher for fs120 tumors ($60.7\pm4.9\mu\text{m}$) compared to fs188 tumors ($45.0\pm4.0\mu\text{m}$). The fs120 tumors also displayed significantly higher vessel tortuosity, fractal dimension and density. The ability to differentiate between tumor types with OCT suggests that the visible abnormal vasculature is representative of the tumor microcirculation, providing a robust, non-invasive method for observing the longitudinal dynamics of the subcutaneous tumor microcirculation.

© 2017 Optical Society of America

OCIS codes: (170.3880) Medical and biological imaging; (110.4500) Optical coherence tomography; (170.2655) Functional monitoring and imaging; (100.2000) Digital image processing.

References and links

- [1] P. Carmeliet and R. K. Jain, "Molecular mechanisms and clinical applications of angiogenesis," *Nature*, vol. 473, pp. 298–307, (2011).
- [2] D. Hanahan and R. A. Weinberg, "Hallmarks of cancer: the next generation," *Cell*, vol. 144, no. 5, pp. 646–74, (2011).
- [3] S. Goel, D. G. Duda, L. Xu, L. L. Munn, Y. Boucher, D. Fukumura, and R. K. Jain, "Normalization of the Vasculature for Treatment of Cancer and Other Diseases," *Physiol. Rev.*, vol. 91, no. 3, (2011).
- [4] A. Puaux, L. C. Ong, Y. Jin, I. Teh, M. Hong, P. K. H. Chow, X. Golay, and J. Abastado, "A Comparison of Imaging Techniques to Monitor Tumor Growth and Cancer Progression in Living Animals," vol. 2011, (2011).
- [5] B. Nico, V. Benagiano, D. Mangieri, N. Maruotti, A. Vacca, and D. Ribatti, "Evaluation of microvascular density in tumors: pro and contra," *Histol. Histopathol.*, vol. 23, no. 5, pp. 601–7, (2008).
- [6] H. A. Lehr, M. Leunig, M. D. Menger, D. Nolte, and K. Messmer, "Dorsal skinfold chamber technique for intravital microscopy in nude mice," *Am. J. Pathol.*, vol. 143, no. 4, pp. 1055–62, (1993).
- [7] B. J. Vakoc, R. M. Lanning, J. A. Tyrrell, T. P. Padera, L. A. Bartlett, T. Stylianopoulos, L. L. Munn, G. J. Tearney, D. Fukumura, R. K. Jain, and B. E. Bouma, "Three-dimensional microscopy of the tumor microenvironment in vivo using optical frequency domain imaging," *Nat. Med.*, vol. 15, no. 10, pp. 1219–23, (2009).

- [8] F. Kiessling, S. Greschus, M. P. Lichy, M. Bock, C. Fink, S. Vosseler, J. Moll, M. M. Mueller, N. E. Fusenig, H. Traupe, and W. Semmler, “Volumetric computed tomography (VCT): a new technology for noninvasive, high-resolution monitoring of tumor angiogenesis,” *Nat. Med.*, vol. 10, no. 10, pp. 1133–8, (2004).
- [9] T. Jeswani and A. R. Padhani, “Imaging tumour angiogenesis,” *Cancer Imaging*, vol. 5, no. 1, pp. 131–8, (2005).
- [10] C. Fink, F. Kiessling, M. Bock, M. P. Lichy, B. Misselwitz, P. Peschke, N. E. Fusenig, R. Grobholz, and S. Delorme, “High-resolution three-dimensional MR angiography of rodent tumors: Morphologic characterization of intratumoral vasculature,” *J. Magn. Reson. Imaging*, vol. 18, no. 1, pp. 59–65, (2003).
- [11] A. Chekkouri, A. Nunes, J. Gateau, P. Symvoulidis, S. V Ovsepian, and A. Walch, “High-Resolution Multispectral Optoacoustic Tomography of the Vascularization and Constitutive Hypoxemia of Cancerous Tumors 1,” *Neo*, vol. 18, no. 8, pp. 459–467, (2016).
- [12] M. P. Wiedeman, “Dimensions of blood vessels from distributing artery to collecting vein,” *Circ. Res.*, vol. 12, pp. 375–378, (1963).
- [13] J. Enfield, E. Jonathan, and M. Leahy, “In vivo imaging of the microcirculation of the volar forearm using correlation mapping optical coherence tomography (cmOCT),” vol. 2, no. 5, pp. 1184–1193, (2011).
- [14] K. Calabro, A. Curtis, J.-R. Galarneau, T. Krucker, and I. J. Bigio, “Gender variations in the optical properties of skin in murine animal models,” *J. Biomed. Opt.*, vol. 16, no. January, p. 011008, (2011).
- [15] A. Mariampillai, M. K. K. Leung, M. Jarvi, B. a Standish, K. Lee, B. C. Wilson, A. Vitkin, and V. X. D. Yang, “Optimized speckle variance OCT imaging of microvasculature,” *Opt. Lett.*, vol. 35, no. 8, pp. 1257–9, (2010).
- [16] G. M. Tozer, S. Akerman, N. A. Cross, P. R. Barber, M. A. Björndahl, O. Greco, S. Harris, S. A. Hill, D. J. Honess, C. R. Ireson, K. L. Pettyjohn, V. E. Prise, C. C. Reyes-Aldasoro, C. Ruhrberg, D. T. Shima, and C. Kanthou, “Blood vessel maturation and response to vascular-disrupting therapy in single vascular endothelial growth factor-A isoform-producing tumors,” *Cancer Res.*, vol. 68, no. 7, pp. 2301–11, (2008).
- [17] M. Guizar-Sicairos, S. T. Thurman, and J. R. Fienup, “Efficient subpixel image registration algorithms,” *Opt. Lett.*, vol. 33, no. 2, pp. 156–8, (2008).
- [18] D. W. Wei, A. J. Deegan, and R. K. Wang, “Automatic motion correction for in vivo human skin optical coherence tomography angiography through combined rigid and nonrigid registration,” *J. Biomed. Opt.*, vol. 22, no. 6, p. 066013, (2017).
- [19] R. A. Byers, G. Tozer, N. J. Brown, and S. J. Matcher, “High-resolution label-free vascular imaging using a commercial, clinically approved dermatological OCT scanner,” in *SPIE BiOS*, (2016).
- [20] A. F. Frangi, W. J. Niessen, K. L. Vincken, and M. A. Viergever, “Multiscale vessel enhancement filtering,” vol. 1496, pp. 130–137, (1998).
- [21] N. Otsu, “A Threshold Selection Method from Gray-Level Histograms,” *IEEE Trans. Syst. Man. Cybern.*, vol. 9, no. 1, pp. 62–66, (1979).
- [22] K. Jurczyszyn, B. J. Osiecka, P. Ziolkowski, & kowski, “The Use of Fractal Dimension Analysis in Estimation of Blood Vessels Shape in Transplantable Mammary Adenocarcinoma in Wistar Rats after Photodynamic Therapy Combined with Cysteine Protease Inhibitors,” *Comput. Math. Methods Med.*, vol. 2012, pp. 1–6, (2012).
- [23] C. O. S. Sorzano, P. Thevenaz, and M. Unser, “Elastic Registration of Biological Images Using Vector-Spline Regularization,” *IEEE Trans. Biomed. Eng.*, vol. 52, no. 4, pp. 652–663, (2005).
- [24] C. Kanthou, G. U. Dachs, D. V. Lefley, A. J. Steele, C. Coralli-Foxon, S. Harris, O. Greco, S. A. Dos Santos, C. C. Reyes-Aldasoro, W. R. English, and G. M. Tozer, “Tumour Cells Expressing Single VEGF Isoforms Display Distinct Growth, Survival and Migration Characteristics,” *PLoS One*, vol. 9, no. 8, p. e104015, (2014).
- [25] J. Xiong, A. Kurz, D. I. Sessler, O. Plattner, R. Christensen, M. Dechert, and T. Ikeda, “Isoflurane produces marked and nonlinear decreases in the vasoconstriction and shivering thresholds.,” *Anesthesiology*, vol. 85, no. 2, pp. 240–5, (1996).
- [26] D. I. Sessler, J. McGuire, J. Hynson, A. Moayeri, and T. Heier, “Thermoregulatory vasoconstriction during isoflurane anesthesia minimally decreases cutaneous heat loss.,” *Anesthesiology*, vol. 76, no. 5, pp. 670–5, (1992).
- [27] U. Baran, W. Wei, J. Xu, X. Qi, W. O. Davis, and R. K. Wang, “Video-rate volumetric optical

- [28] coherence tomography-based microangiography,” Opt. Eng., vol. 55, no. 4, p. 040503, (2016).
- [28] Z. Zhi, W. Qin, J. Wang, W. Wei, and R. K. Wang, “4D optical coherence tomography-based micro-angiography achieved by 16-MHz FDML swept source,” Opt. Lett., vol. 40, no. 8, p. 1779, (2015).
- [29] L. S. Hansen, J. E. Coggle, J. Wells, and M. W. Charles, “The influence of the hair cycle on the thickness of mouse skin,” Anat. Rec., vol. 210, no. 4, pp. 569–573, (1984).
- [30] W. R. English, S. J. Lunt, M. Fisher, D. V Lefley, M. Dhingra, Y.-C. Lee, K. Bingham, J. E. Hurrell, S. K. Lyons, C. Kanthou, and G. M. Tozer, “Differential Expression of VEGFA Isoforms Regulates Metastasis and Response to Anti-VEGFA Therapy in Sarcoma,” Cancer Res., p. canres.0255.2016, (2017).
- [31] H. Kämpfer, J. Pfeilschifter, and S. Frank, “Expressional regulation of angiopoietin-1 and -2 and the tie-1 and -2 receptor tyrosine kinases during cutaneous wound healing: a comparative study of normal and impaired repair.,” Lab. Invest., vol. 81, no. 3, pp. 361–73, (2001).
- [32] N. M. Biel, J. a Lee, B. S. Sorg, and D. W. Siemann, “Limitations of the dorsal skinfold window chamber model in evaluating anti-angiogenic therapy during early phase of angiogenesis.,” Vasc. Cell, vol. 6, no. 1, p. 17, (2014).

1. Introduction

Within the body, the structural features of major arteries and veins are genetically controlled during embryonic development and generally remain consistent between individuals. The microvasculature however can be dynamically remodeled as a result of molecular and mechanical stimuli within the local microenvironment[1]. Tumor growth relies on a continual process of micro-vascularization, notably via angiogenesis, which also facilitates metastasis[2]. The resulting tumor vasculature is both morphologically and functionally abnormal[3], the study of which potentially offers valuable insight into tumor development and pathophysiology.

Angiographic imaging of murine models of cancer has proved particularly important to oncological research, greatly aiding our understanding of tumor growth, progression and treatment within living animals[4]. Traditional necropsy methods such as immunohistochemistry have retained their importance for quantifying the microcirculation within implanted tumors[5]. However modern non-invasive imaging techniques have quickly gained traction due to the potential of longitudinal vascular visualization, vastly reducing the number of animals required to produce statistically robust data. Currently, intravital microscopy is widely utilized to study tumor growth, typically involving the surgical replacement of the highly scattering skin layer with a transparent glass coverslip[6]. Using this model, angiographic optical coherence tomography (OCT) imaging has been used to enable high-resolution longitudinal imaging of tumor dynamics and response to treatment[7]. Furthermore, in-vivo full field angiography of subcutaneously grown tumors, with overlying skin intact, has previously been achieved with perfusion computed tomography[8] and dynamic magnetic resonance imaging[9], [10]. More recently, multi-spectral optoacoustic tomography has been utilized to visualize vascular morphology and oxygenation at 70 μm resolution over entire 1cm³ tumor volumes[11].

Despite these advances, it remains challenging to non-invasively image the microscale circulation within subcutaneously implanted tumors because optical modalities are required to resolve these vessels (typically 5-50 μm in diameter[12]), and these modalities are often unable to penetrate through the highly scattering layer of skin. OCT is an established imaging technique which has been widely utilized to capture both structural and angiographic images within human skin[13]. Most notably, OCT offers depth penetration of up to ~1mm within tissue and is capable of extracting depth encoded data such that individual layers of tissue can be visualized at a high resolution. Compared to human skin, which can be many millimeters thick; female CD-1 nude mice generally exhibit superficial tissue layers approximately ~550 μm in thickness (~30 μm epidermis, ~220 μm dermis, ~300 μm hypodermis)[14]; thus the superficial vasculature of subcutaneously implanted tumors may be visible and within the field of view of

OCT. Speckle-variance OCT (svOCT) can be used to extract volumetric flow information from four-dimensional OCT data sets (X-Y-Z-Time), with multiple data points being collected at each spatial location[15]. This is based on the fact that a fluid pixel will display rapidly evolving temporal variations in the OCT signal (speckle patterns) when compared to solid tissue pixels. Hence by calculating the variance of pixels at the same spatial location as a function of time, contrast is generated between stationary solids and moving liquids.

This study aimed to develop and evaluate the performance of angiographic svOCT in the context of murine subcutaneous tumor imaging. In particular, we attempt to differentiate the vascular morphologies within mouse tumors derived from fibrosarcoma cells genetically engineered to express only single splice variant isoforms of vascular endothelial growth factor A (VEGF); either VEGF120 or VEGF188 (fs120 and fs188 tumors respectively). Previously, using tumors grown in transparent chambers implanted into the rear dorsum of mice and conventional intravital optical microscopy, we observed that fs120 tumor blood vessels were larger, more disorganized and formed more tortuous vascular networks than those of fs188 tumors[16]. This study aimed to identify whether these differential vascular patterns were also present within the microcirculation of subcutaneously grown tumors, independent of the dorsal skin-fold window chamber.

2. Materials and methods

All animal experiments were conducted according to the United Kingdom Animals (Scientific Procedures) Act 1986 (UK Home Office Project License PPL40/3649) and with local University of Sheffield ethical approval.

2.1 Subcutaneous tumor implantation

In order to evaluate the capabilities of OCT for the imaging of subcutaneously implanted tumors, mouse fibrosarcoma tumor cells (1×10^6 in 0.05 ml serum-free Dulbecco's Minimal Essential Medium) expressing VEGF as only its highly soluble VEGF120 isoform (fs120 tumor cells) or its highly matrix-bound isoform VEGF188 (fs188 tumor cells) were subcutaneously injected into the rear dorsum of female CD1 nude mice aged 8-12 weeks. Development of these cell lines has been described previously[16]. Female nude mice were chosen due to their absence of hair, and having slightly thinner dermis/hypodermis skin layers than male nude mice[14]. OCT imaging of each tumor was performed daily, with the mice under isoflurane anesthesia. Daily caliper measurements were made of the three orthogonal tumor diameters and animals were sacrificed once the largest tumor diameter reached no more than 12mm. Excised tumors with overlying skin intact were halved and fixed in 10% neutral buffered formalin overnight and then paraffin-embedded prior to processing for histological analysis with hematoxylin and eosin (H&E) staining and immunohistochemistry for rat anti-mouse cluster of differentiation 31 (CD31) monoclonal antibodies (Cat No. DIA-310, Dianova GmbH, Hamburg, Germany), as a marker of vascular endothelial cells.

2.2 Data acquisition and imaging protocol

All imaging for this study was performed using a commercial CE-marked multi-beam OCT system (Vivosight®, Michelson Diagnostics Ltd, Orpington, Kent, UK). This system utilizes a swept-source 1305nm Axsun laser with a bandwidth of 147nm, achieving a resolution of approximately 5 μ m axially and 7.5 μ m laterally (In tissue). One-dimensional A-scans are captured at a line rate of 20 kHz and contain structural information to a depth of approximately 1mm in murine skin. The imaging beam is scanned laterally across the surface of the tumor in order to collect a 3-dimensional image. In an effort to reduce the degree of motion within the collected OCT scans, the mobile imaging probe of the Vivosight was clamped into position and manually lowered to the correct height. A plastic standoff bridged the gap between the imaging probe and the skin. The standoff gently contacted the skin surface such that any lateral

movement was reduced. Fixation of the imaging probe in this manner is important as it removes a source of movement from the resulting data. In order to minimize homeostatic effects on the circulation as a result of temperature variation, the rectal temperature of the mouse was maintained at 37°C during imaging using a heating mat which was thermostatically controlled via a rectal thermocouple probe. Furthermore, all imaging was conducted inside a plastic chamber which was heated to an internal temperature of 32°C. This experimental setup is illustrated in fig. 1.

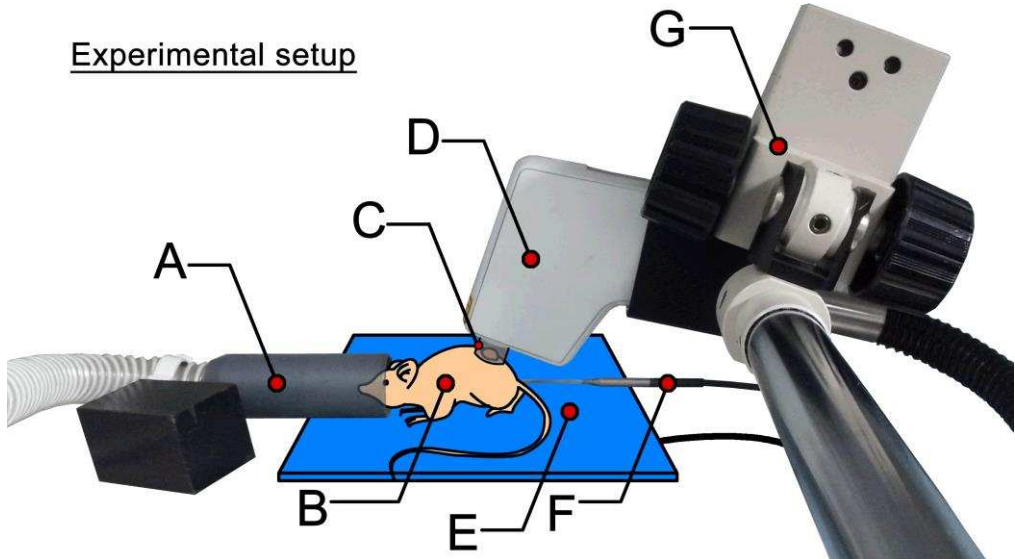


Fig. 1. Experimental setup within a plastic chamber which was heated to 32°C internal temperature. A) Rodent facemask for administration of isoflurane gaseous anesthesia. B) CD-1 Nude mouse. C) Plastic standoff which gently contacts the skin around the subcutaneous tumor. D) The OCT imaging probe (Vivosight). E) Feedback controlled heated mat. F) Rectal temperature probe (Feeds back to the heated mat). G) Mobile clamp for repositioning of the OCT imaging probe.

For this study, the scan size was set at 6mm in both the x and y directions, giving a wide field of view across the tumor. The spacing between A-scans was fixed at 10 μ m in order to closely match the lateral resolution of the OCT system while maintaining a high scan speed. Five repeat frames ($N = 5$) were collected at each stepped y-location and later used to evaluate the speckle-variance within each voxel. With these settings, each dataset took approximately 90 seconds to acquire, the raw data was stored to disk and processed offline.

2.3 Post-processing of data

Following data acquisition, data processing was performed externally within MATLAB (R2015b – MathWorks). To minimize processing time, each stack of B-scans was processed in parallel using a graphical processing unit (GPU) (NVIDIA GeForce GTX 780) with 4GBytes of RAM. This was achieved through utilization of the parallel computing toolbox within MATLAB.

Directly following the resampling of raw OCT data into image space there are numerous post processing steps that were performed in order to maximize the contrast of the svOCT images and reduce the influence of motion artefacts on the resulting visualization. Firstly, a sub-pixel accurate image registration algorithm was applied in order to register frames within each stack (100th of a pixel accuracy). This attenuates unwanted subject movement within the B-scan plane. For this, a cross-correlation based algorithm initially described by Guizar et al[17] was selected and modified to utilize the GPU's architecture. This algorithm uses a

selectively upsampled discrete Fourier transform as opposed to a zero-padded fast Fourier transform in order to reduce the required computational time and memory without negatively affecting the accuracy of registration; this is ideal for GPU computing as memory usage is typically a limiting factor. After registration, each repeat frame within the stack ($N=5$ frames at each location) was assigned a score equal to its average correlation to each of the other frames within the stack. The frame with the highest score was then assigned as the best candidate for a base frame. Following this, the k frames within the stack which exhibit the highest correlation with the base frame were retained, with any other frames being discarded. For simplicity, the parameter k was defined as half the stack size rounded up, so in the case of 5 repeat frames at each location, 3 frames were retained for further processing. This process, repeated across each stack of repeat images served to retain a proportion of the data that was least likely to be corrupted by motion artefacts without requiring the assignment of a dynamic correlation threshold value. These registration techniques are similar to those utilized in previous work[18], and are an effective method of reducing motion derived artefacts.

Following this correlation optimization step, the speckle-variance signal is calculated from the remaining 4-dimensional image data using a variance equation adapted from previous work by Mariampillai et al[15] (Eq.1).

$$SV(x, y, z) = \text{median}((I(x, y, z, n) - \frac{1}{k} \sum_{n=1}^k I(x, y, z, n))^2) \quad (1)$$

x, y and z correspond to voxel indices, n represents the frame index within each B-scan stack and I is the corresponding pixel intensity at a particular spatial location. The 1D median function is performed across each stack ($n=1:k$) and serves to attenuate outlier values of variance, such as those caused by sudden interface movements.

A thresholding process was then performed to remove noise-dominated areas containing little to no information regarding the structural properties of the tissue. For this, each stack of B-scans was averaged and 2D Gaussian filtered with kernel size 5×5 and a standard deviation of 2 pixels. A mask was then generated through binary segmentation of the resulting images, with the threshold being defined as the 95th percentile of pixel intensities situated within the 10 deepest image rows. The lower rows were selected as they typically exhibit close to zero structural signal, instead consisting entirely of noise. This mask was applied to the corresponding svOCT image, deleting areas that contained negligible OCT signal.

The next step involved flattening the skin surface level such that vascular plexus could be projected onto a flat horizontal plane. This is required as the murine skin is very rarely flat on the surface, instead consisting of various epidermal ridges. Noise and bright artefacts originating at the interface between the stratum corneum and air make it challenging to accurately segment the surface of the skin. Hence surface detection was achieved using the averaged B-scans that were previously used for thresholding purposes. For this, a mask was generated by considering the differential between pixels in the depth (z) direction of the B-scan images; highlighting only regions with a significant increase (dark to bright) in intensity. Morphological area opening was then applied to this mask to remove any detected regions which were below 50 pixels in size. The most superficial detections for each column (z) were recorded and any gaps in the resulting surface line were interpolated across (cubic-spline). This process was repeated for each of the B-scan stacks, with the 2D surface detections being combined to produce a 3D surface plot. Lastly the detected surface was 2D median filtered with a 20×20 kernel to eliminate outliers and then used to axially shift each A-scan of the svOCT data to a certain predefined surface depth.

Despite the previous processing steps, strong vertical motion artefacts remained visible on the en-face images of the tumor vasculature. These arise because of global decorrelation caused by the animals breathing, heartbeat or muscular spasms during the imaging process. To improve visualization of the data and enable accurate quantification of vascular morphology to be performed, it was necessary to remove these artefacts. Previous publications have utilized

consecutively acquired 3D volumes and vessel layer segmentation in order to mosaic and eliminate such vertical bands with no notable image degradation[18], providing they are at a different location on each consecutive scan. However, to avoid doubling the required scan time for each volume, these bands were instead removed entirely through software. This was achieved using a combined wavelet-FFT filter similar to that previously described[19]. Briefly, the filter attenuates high frequency components along the y-direction of the OCT volume, notably the sharp decorrelations caused by movement, which result in similarly sharp spikes in svOCT image intensity. Such vertical components are separated from the underlying detailed image using a multi-level Daubechies wavelet transform. Each “vertical” image from the wavelet decomposition was then 2D Fourier transformed and the central frequencies surrounding the x-axis were attenuated through application of a 11-pixel high mask, designed to remove non-uniform (in y) vertical line artefacts. The vertical image is then inverse Fourier transformed and recombined with its corresponding “horizontal” and “detail” images using successive inverse wavelet transforms. While removal of perfect vertical artefacts is achievable simply using the Fourier transform, the additional wavelet transformations allowed for imperfect artefacts to be removed with minimal effect on the underlying detail. Fig. 2 shows the result of wavelet filtering on the vasculature of an fs188 tumor. Since the vertical lines are effectively being blurred in the y-direction (due to the attenuation of high frequency y-components in the image), this process can result in visible banding within the background intensity of the image, particularly around areas which contained wide or numerous line artefacts. Despite these banding artefacts, the underlying image clarity was greatly improved and binarization was able to be performed without the anomalous detection of the strong vertical lines (Sec. 2.4).

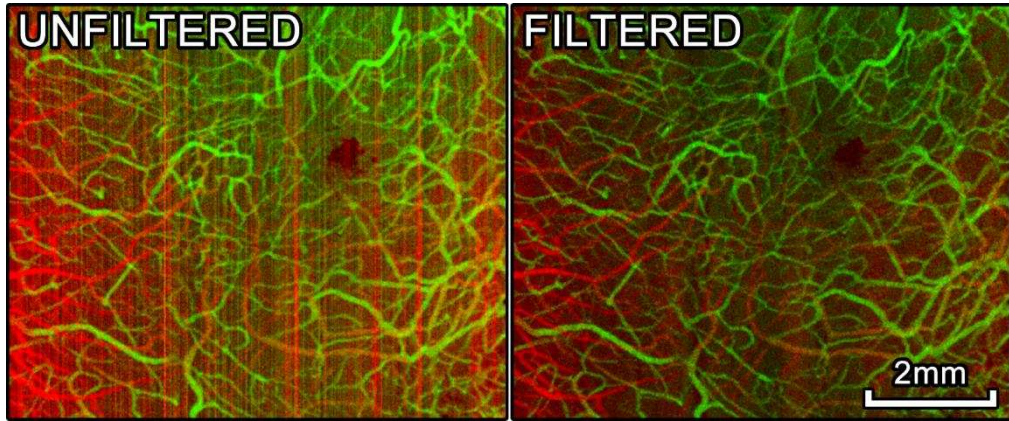


Fig. 2. En-face svOCT images of an fs188 tumor before (Left) and after (Right) wavelet/FFT filtering was performed using a Daubechies wavelet to a decomposition level of 5. The colors correspond to the depth of the detected vessels, red vessels are 0-300 μm and green vessels are 300-600 μm beneath the skin surface.

Following post-processing, as described above, the resulting SV matrix contains 3-dimensional information pertaining to the location of the microvasculature.

2.4 Quantification of vessel parameters

Quantification of vessel parameters required binarization of each angiographic image such that a vascular skeleton could be generated. For this, volume projections of the OCT datasets were generated by performing a mean-intensity projection (MIP) over the depth range 0-800 μm . The resulting angiographic OCT images were often noisy, with both vessels and background being highly non-uniform in pixel intensity (fig. 3B). As a result of this, simple intensity thresholds

are challenging to assign, generally yielding an overly complex skeleton with noise being anomalously detected as vasculature. To address this issue, the images were median filtered with a 3x3 kernel before being processed with a multiscale Hessian filtering algorithm[20]. This algorithm attempts to measure the “vesselness” of a pixel through consideration of the eigenvalues of the local Hessian matrix, assigning a value close to 1 for regions which are tubular in nature and 0 for regions which remain flat. To minimize any artificial vessel dilation or constriction in the resulting image it was necessary to repeat this process over a range of vessel scales (5-100 μ m), with the maximum filter value for each pixel being recorded (fig. 3C). The filtered image was then pixel-wise multiplied by the original image to suppress the background noise and improve contrast (fig. 3D). This combined image was then binarized using an automatically defined Otsu threshold[21] before being skeletonized (fig. 3E/F).

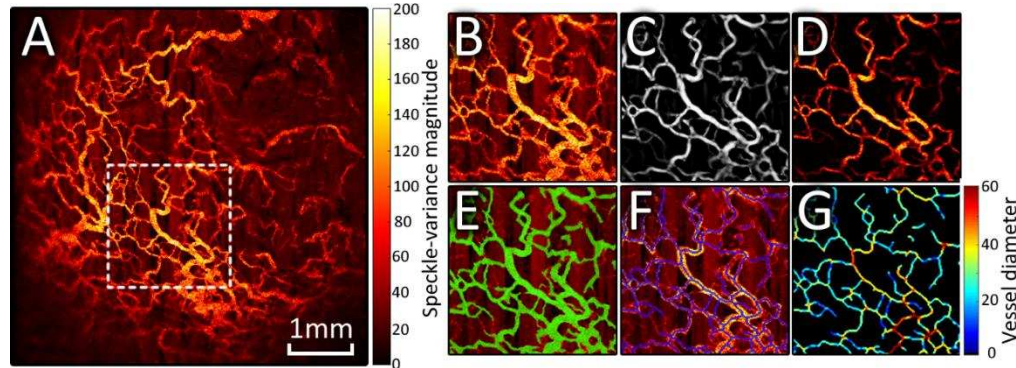


Fig. 3. Processing steps for the quantification of svOCT data. A) En-face svOCT image captured from a subcutaneous fs-120 tumor 17 days post-implantation. Dashed box shows zoomed section from B-G. B) Zoomed section of the en-face svOCT image. C) The result of the hessian-based filtering algorithm. D) The result of B*C, improved vascular contrast against the background. E) Binary threshold in green overlaid on the original image. F) Skeleton in blue overlaid on the original image. G) Map of vessel diameter calculated using the binary threshold and the skeleton data from E and F.

A user defined field-of-view was used for quantification to ensure that only representative areas were selected. Areas of expected low angiographic signal such as the corners or gaps/holes in the image were discarded. Using the skeleton and binary data, vessel diameter was defined at each point on the skeleton as width of the binarized data perpendicular to the skeleton, a mean vessel diameter was then calculated by averaging across all skeleton points within the field-of-view. Total vessel length per mm² was calculated by averaging the total length of skeleton contained within 1mm² sub-blocks of the image. Vessel density (%) was simply the percentage of pixels within the field-of-view that were identified as vascular. Tortuosity was calculated as the average ratio between shortest path length and Euclidean distance between distant end-points at opposite sides of the skeleton. To calculate vessel segment length, the skeleton was broken into vessel segments by removing bifurcation points from the network, segment length was then defined as the path length between segment end points. Lastly, the fractal dimension of the skeleton was calculated using the box-counting method, resulting in a value between 0 and 3, with lower values indicating a more regular network[22].

For the longitudinal comparison of svOCT images captured from the same tumor over a period of time (Section 3.2), elastic image registration was performed in order to ensure accurate vessel correlation between frames. This was achieved using a vector-spline method which has been detailed previously[23].

2.5 Statistics

Statistical analysis was carried out using MATLAB (R2014b – Mathworks). The unpaired Students t-test was used to test for significant differences between the two tumor types (fs188 and fs120). For cases where comparisons were made between three groups (Healthy, fs188 and fs120) a one-way ANOVA followed by the Tukey-Kramer honest significance difference (HSD) test was used. In all cases, comparisons were described as significant if the probability of the null hypothesis was <0.05 . All stated measurements are of the form mean \pm SD.

3. Results and discussion

3.1 Visual inspection of VEGF120 and 188 expressing tumors

Fig. 4 shows a selection of en-face depth encoded svOCT images captured from both baseline skin and the subcutaneously implanted tumors of CD1 nude mice.

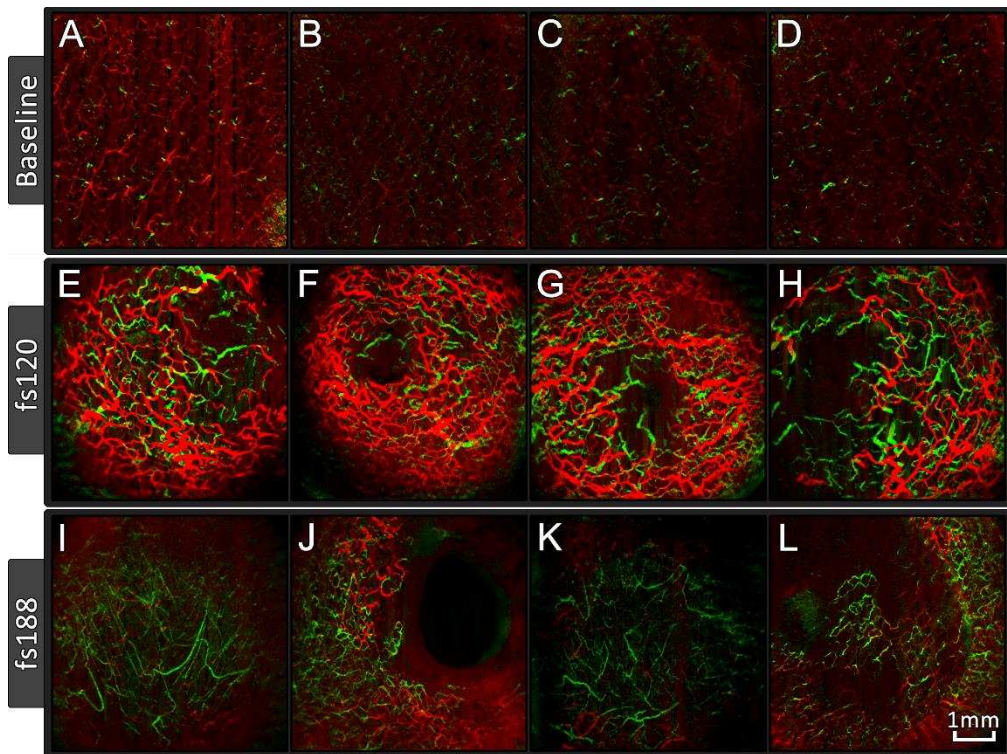


Fig. 4. A selection of 6x6mm en-face svOCT images. A-D) Images of baseline murine skin vasculature without the presence of a tumor. E-L) Images of established subcutaneous tumor vasculature, each image is of a separate tumor captured once the largest tumor diameter exceeded 10mm. Middle row (E-H) shows tumors expressing only the VEGF120 isoform (fs120) and bottom row (I-L) shows tumors expressing only the VEGF188 isoform (fs188). All images were captured from different animals. The colors correspond to the depth of the detected vessels, red vessels are 0-400 μ m and green vessels are 400-800 μ m beneath the skin surface. E-L) Number of days post-implantation > 14 days.

The large abnormal vessel networks such as those seen in fig. 4E-L only became visible to svOCT approximately 8-15 days post implantation. Prior to this, more regular organized vessel networks as represented in fig. 4A-D were visible. This suggests that the early stages of tumor vessel development remain too deep within the tissue to be effectively imaged by OCT. However, after sufficient tumor expansion, typically ~10-days post-implantation, large

abnormal vessels were clearly visible within the field-of-view of the OCT system. This longitudinal vascular growth is further discussed in section 3.2. Interestingly, the baseline vasculature appeared to be absent from the late-stage scans as evidenced by a comparatively lower angiographic signal at the “red depth” (0-400 μ m) aside from that attributed to larger abnormal vessels, suggesting that as the skin stretches over the surface of the tumor the flow in regular vessels ceases. Furthermore, it appears that the fs120 tumors are more infiltrative than the fs188 variants, with a large portion of abnormal vessels appearing at superficial depths within skin. This is clearly visible in fig. 4, where a large portion of the fs120 vessels appear red (0-400 μ m depth), whereas the majority of the fs188 vessels appear green (400-800 μ m). This effect may be related to the distinct phenotype of the fibrosarcoma cells, with fs120 cells demonstrating a more proliferative phenotype than the fs188 variants both in-vitro and in-vivo. Furthermore, fs120 tumors have an additional ability to adopt both mesenchymal and amoeboid morphologies, which is considered an advantage for invasion[24]. One limitation of the svOCT technique is an observed shadowing effect beneath detected vessels caused by the forward scattering of photons by blood, which can occlude underlying vasculature[7]. For the case of the fs120 tumors, many of the vessels which are likely to be at the 400-800 μ m depth range (Green) are occluded by more superficial vessels at the 0-400 μ m depth range (Red), making vessels density calculations challenging to perform at an equivalent depth. This limitation is discussed further in section 3.3.

3.2 Evaluation of longitudinal tumor monitoring

One key advantage of non-invasive subcutaneous tumor imaging is the potential for longitudinal observation of tumor growth and vascular development. Fig. 5 shows an example of longitudinal data acquisition, with images being acquired from the same fs120 and fs188 tumors over a period of 5 days, as well as a longer timescale visualization of vascular development within an fs188 tumour from days 0 to 15.

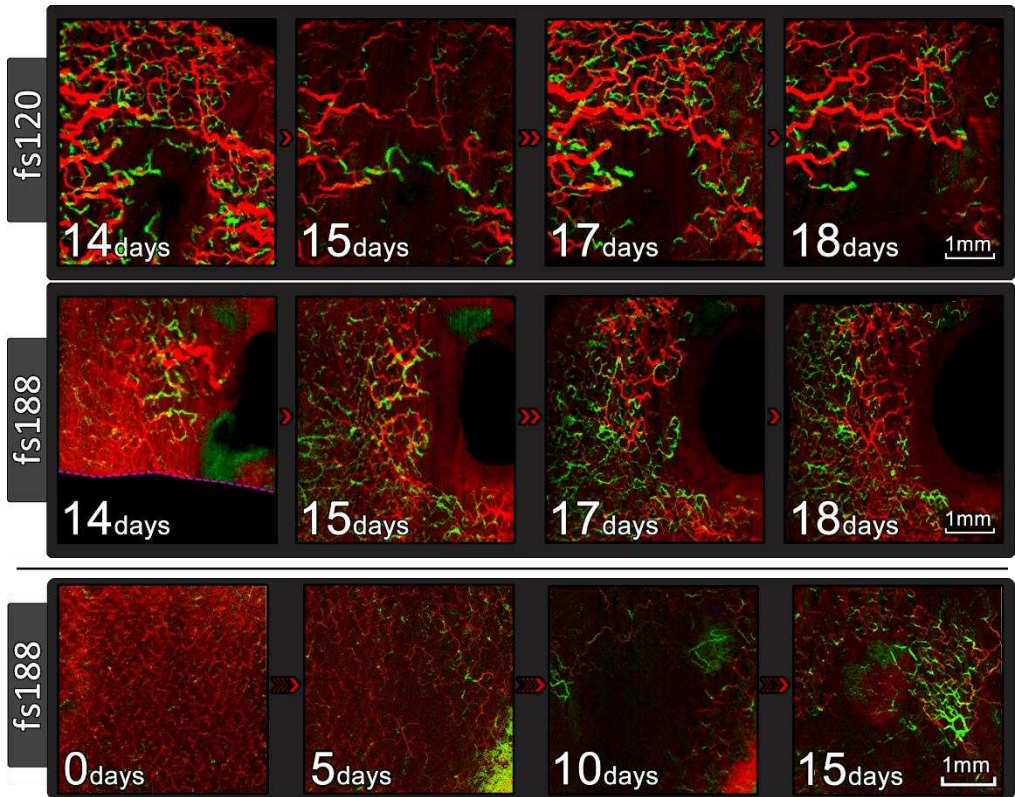


Figure 5. Top and middle rows) Depth encoded short-term longitudinal svOCT images of both an fs120 and an fs188 tumor over a period of 5 days. Images have been elastically registered together using UnwarpJ[23] such that the same vessels align on subsequent frames. Bottom row) 4x4mm (Zoomed) en-face svOCT images showing long-term longitudinal vascular progression from pre-tumor implantation to 15-days post-tumor implantation. Each separate row represents longitudinal data that was captured from one unique animal. The colors correspond to the depth of the detected vessels, red vessels are 0-400 μm and green vessels are 400-800 μm beneath the skin surface. The white number in the lower left corner of each image corresponds to the number of days post-tumor implantation that the image was captured.

The scans have been elastically co-registered such that vessels are aligned, following a similar methodology to that detailed previously[18]. For the case of the fs120 tumor, the mean vessel length per mm^2 is highest at day 14 post-implantation (4.1mm^{-1}), it then decreases to 1.4mm^{-1} at day 15, recovers to 3.5mm^{-1} on day 17 before decreasing again to 2.1mm^{-1} on day 18. Comparatively the fs188 tumor rises from 1.1mm^{-1} on day 14 (excluding the lower region which was outside of the scan field-of-view), to 2.2mm^{-1} on day 15, reduces to 2.0mm^{-1} on day 17, before returning to 2.2mm^{-1} at day 18. To investigate this effect over a larger sample size, the standard deviation of mean vessel length per mm^2 was calculated for each tumor within both the fs120 and fs188 cohorts over days 14 to 18 post-implantation. A two-sample independent t-test was then used to evaluate significance. A majority of the tumors had unsuitable datasets and thus were omitted from this analysis. Omission was a result of either the data having a non-complimentary field of view (non-overlapping scan site on subsequent days), or certain days displaying motion corrupted vascular signal, both being unsuitable for comparison. In total, the number of viable datasets used was $n=4$ for both the fs120 and fs188 groups. Whilst the fs120 group had a higher variation in measured vessel lengths over time ($\text{SD} = 1.4\text{mm}^{-1}$) when compared to the fs188 group ($\text{SD} = 0.4\text{mm}^{-1}$), this result did not reach statistical significance ($p=0.063$) due to the small sample number. Thus it is unclear if fs120

tumors demonstrate increased day-day variation in mean vessel length. Fig. 6 shows the changes in mean vessel length per mm^2 for each animal over time.

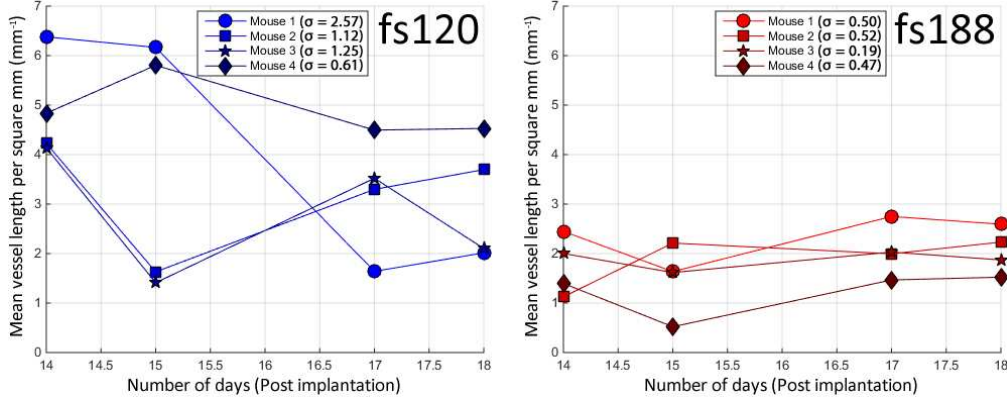


Fig. 6. Line plots showing the variation in measured vessel length per square mm as a function of time within subcutaneous tumors expressing either the VEGF120 isoform (blue) or the VEGF188 isoform (red). The standard deviation in the measured mean vessel length for each animal is calculated as a function of time, and represents how much variance is visible within the measurement. The average of these standard deviations across all four fs120 mice (1.4mm^{-1}) is higher than those in the fs188 cohort (0.4mm^{-1}), however this result does not reach statistical significance ($p = 0.063$).

Such variability in the number of visible vessels from one day to the next is unlikely to be a result of vascular remodeling. It could potentially be a direct result of increased pressure being applied to the surface by the plastic standoff cap on these days (Seen in fig. 1C). However, in this case the more superficial (red) vessels might be expected to occlude, which does not appear to be the case. Alternatively, it is possible that reduced localized flow within the disappearing vessel linkages is responsible for the loss of visualization, as if the decorrelation time of the slow-flowing blood reduces below the frame acquisition interval (~30ms) of the OCT system, then the flow signal is lost. Another explanation for the loss of vessel density is that vasoconstriction or upstream vascular shunting may be occurring as the region homeostatically responds to small changes in external stimuli such as temperature. It is also highly likely that the use of isoflurane anaesthetic is both influencing the degree of thermoregulatory inhibition and acting as a cardiovascular depressant, reducing the blood pressure [25], [26]. For this study, given the relatively low volume acquisition rate of the Vivosight OCT system (0.01 Hz), it was not feasible to perform angiographic imaging of solid tumors without the use of anaesthetic. Recent developments in MHz range swept source lasers have enabled angiographic OCT volume scans to be acquired at video rate (1-25 Hz)[27], [28]. This may enable high-speed imaging of the subcutaneous tumor microcirculation without the requirement of anesthetic.

3.3 Evaluation of OCT depth penetration

Fig. 7 shows a direct comparison between the OCT B-scans and histological samples taken from the rear-dorsum of CD1 nude mice. In healthy skin (fig. 7A/B) a thick hypodermis layer (~400 μm) is filled with dense hair follicles which scatter the incident 1300nm OCT beam, preventing the light from penetrating deeper into the tissue. A thin section of the striated muscle layer is visible to the right side of the OCT image, but structures are not discernable beneath this layer.

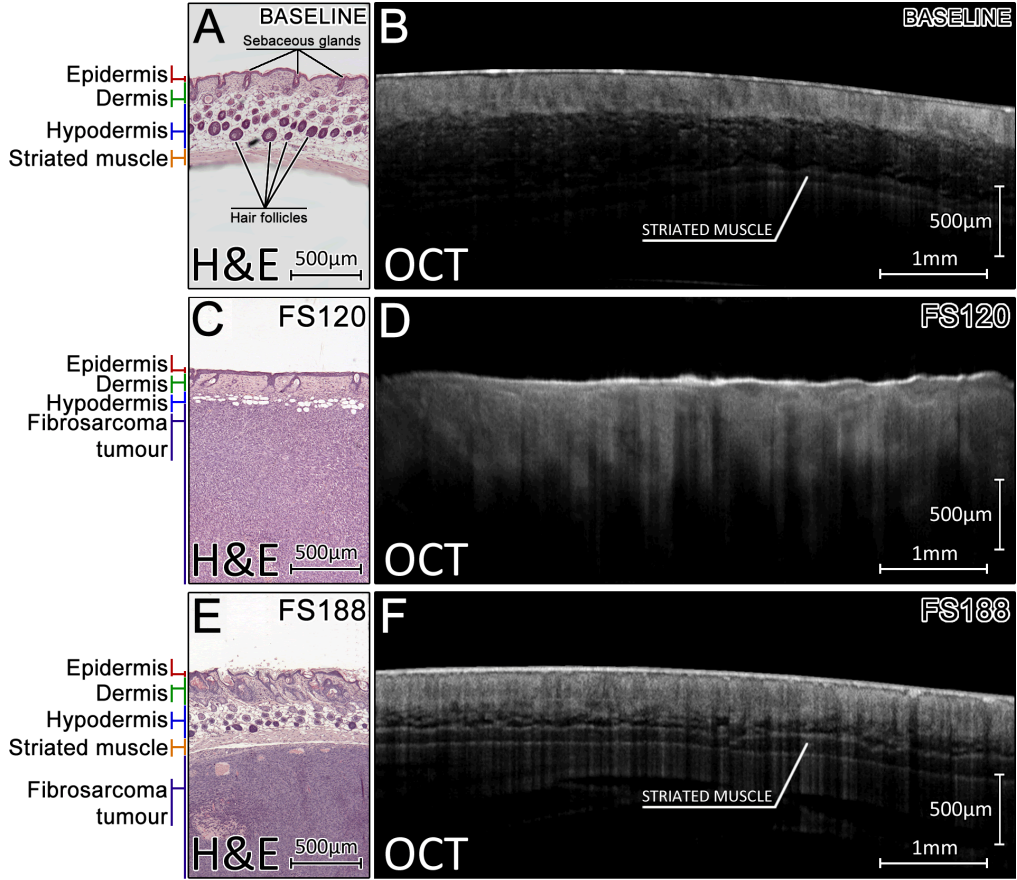


Fig. 7. Comparing the depth penetration of OCT against histological sections of murine rear-dorsum skin. A) H&E stained section of healthy skin. B) OCT B-scan of healthy skin (Different animal to A). C) H&E stained section of the skin above an fs120 tumor, showing the lack of the muscular layer. D) OCT B-scan of the skin above an fs120 tumor (Same animal as C). E) H&E stained section of skin with an fs188 tumor visible beneath the muscular (panniculus carnosus) layer of the skin. F) OCT B-scan of the skin above an fs188 tumor (Same animal as E).

While the thickness of the hypodermis within murine skin is known to be modulated by the hair cycle[29], the presence of a tumor has clearly altered the outer skin morphology (fig. 7C/E). To investigate this, multiple measurements of the hypodermal thickness were acquired from sections of skin. Given the variable contrast of the hypodermis on the cross-sectional OCT images, particularly for the fs120 tumors (fig. 7D), these measurements were made using histological sections of the skin. For each unique skin section, the upper and lower layer of the hypodermis were manually traced within MATLAB (R2015b – MathWorks), an average value of hypodermis thickness was then calculated by considering the vertical distance between these upper and lower boundaries. These measurements of hypodermis thickness were acquired from healthy skin ($n=7$) and compared to similar measurements acquired from skin surrounding the fs188 and fs120 tumors at the end of the study ($n=7$ per group). A balanced one-way ANOVA was performed between the three groups, followed by the Tukey-Kramer HSD test to evaluate significance, these results are summarized in fig. 8.

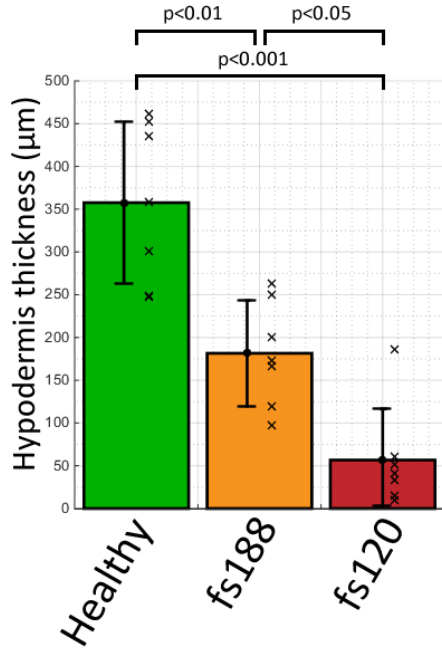


Fig. 8. Variation in the thickness of the hypodermis (fat) layer within healthy skin compared to that of the skin encapsulating ~12mm diameter fs188 and fs120 tumors. The fatty layer is significantly thicker in healthy skin than both fs188 and fs120 skin, furthermore this layer is also significantly thicker in fs188 skin than fs120 skin. A thicker fat layer appears to correlate with an increase in the number of hair follicles present, reducing the depth penetration of the OCT imaging beam. (columns, mean; bars, standard deviation; crosses, datapoints). All groups contain n=7 samples, significance calculated using a one-way ANOVA followed by a Tukey-Kramer HSD test.

The thickness of the hypodermis was found to be significantly greater in healthy skin ($357 \pm 94 \mu\text{m}$) compared to that of skin covering an fs188 tumor ($182 \pm 62 \mu\text{m}$, $p < 0.01$) or fs120 tumor ($57 \pm 60 \mu\text{m}$, $p < 0.001$). There was also a significant reduction in skin thickness between the fs188 and fs120 groups ($p = 0.015$), which could be caused by abnormal strains placed on the skin as it stretches over the growing tumor. An example of the thinned hypodermis is seen for the fs188 tumor (fig. 7E/F); in these cases OCT is able to capture the upper layers of skin (epidermis, dermis), the adipose layer of fat cells (hypodermis), the muscular layer and approximately $500 \mu\text{m}$ deep into the fs188 tumor, representing a total depth penetration of ~1mm. Fig. 7C/D show similar comparisons for an fs120 tumor. Interestingly, most fs120 tumors exhibited a unique skin morphology in that the layer of striated muscle was absent and in some extreme cases the hypodermis was also heavily disrupted, with adipocytes scattered within the tumor, there was also a notable absence of hair follicles within the hypodermis (fig. 7C). This could again be indicative of the more invasive phenotype of this tumor type[24]. In such cases, the remaining layers of superficial skin were ~ $200 \mu\text{m}$ thick, consisting of only the epidermis, dermis and extremely thinned hypodermis. This resulted in a much deeper view into the tumor tissue with OCT as seen in fig. 7D, potentially explaining why large abnormal tumor vasculature was visible at superficial depths of less than $300 \mu\text{m}$ in fig. 4.

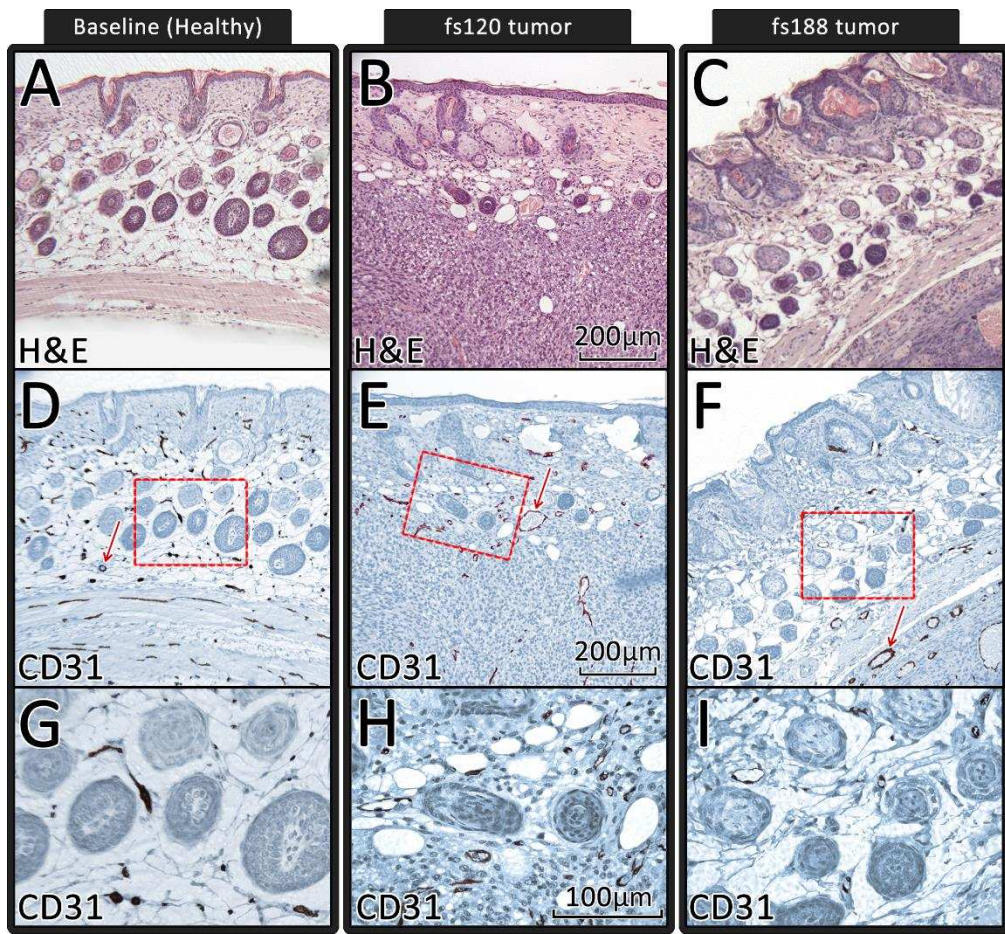


Fig. 9. CD31 immunohistochemistry demonstrating the presence of endothelial cells lining the vessels within the rear-dorsum skin of CD1 nude mice. A-C) H&E stained serial sections of healthy, fs120 and fs188 skin respectively. D-F) CD31 immunostained serial sections of healthy, fs120 and fs188 skin respectively. Endothelial cells are stained in brown. Red arrows represent the largest visible vessel lumen. Red boxes represent the zoomed sections from G-I. G-I) Zoomed view of vessels within the hypodermis of the CD31 stained sections. The fs120 tumor shown here was excised 14 days post-implantation and is a different tumor to the one shown in figure 9. The fs188 tumor shown here was excised 20 days post-implantation, and is the same tumor shown in figure 9.

Fig. 9 shows a comparison between H&E and CD31 stained sections of healthy, fs120 and fs188 skin. In the case of healthy skin (fig. 9A/D/G), CD31 immunostaining has highlighted the presence of vascular endothelial cells throughout the dermis, hypodermis and striated muscle layers of the murine skin. The largest visible vessel lumen, highlighted by the red arrow is approximately 15 μm in diameter. For the skin containing an fs120 tumor (fig. 9B/E/H), the majority of vessels are visible at the periphery of the tumor, the largest of which is ~65 μm in diameter (red arrow). For the skin overlying an fs188 tumor (fig. 9C/F/I), there is still evidence of vascularization within the dermis/hypodermis, however the majority of visible vessels are inside the tumor, directly below the striated muscle layer at a depth of ~600 μm , the largest of which is ~50 μm in diameter (red arrow). These are likely to be the vessels which appeared green on fig. 4. Fs120 tumor cells have clearly invaded deep into the hypodermis, whereas the fs188 tumor remains contained beneath the striated muscle layer. Due to the increased

infiltration of the fs120 tumors, these vessels are situated at a depth of 300 μm and appear red on the depth resolved OCT scans shown in fig. 4.

In general, depth penetration appears sufficient to capture the superficial layers of vasculature within both fs120 and fs188 tumors. However, achieving high axial depth penetration at a particular location remains dependent on the absence of highly scattering structures in the upper skin layers. Shadows from superficial scattering structures such as hair follicles can be seen as a banding pattern on fig. 7B/D/F, and may occlude the angiographic signal from vessels directly below the structure.

3.4 Quantitative vessel metrics

Fig. 10 shows the variation of each of the quantitative parameters detailed in section 2.4 as a function of tumor type at study endpoint. Independent two-sample t-tests were used to calculate significance between the tumor types, with the significance levels between tumor types being listed above each graph. Mean vessel diameter was significantly higher for the fs120 tumors ($60.7 \pm 4.9 \mu\text{m}$) than the fs188 tumors ($45.0 \pm 4.0 \mu\text{m}$), an observation which agrees with previous intravital observations of the same tumor types grown in window-chambers[16]. It is likely that measured vessel diameters below 20 μm are overestimated when viewed through OCT, due in part to spatial aliasing. Given that the OCT datasets for this study were acquired with lateral spacing ($\Delta x, \Delta y$) of 10 μm , Nyquist sampling suggests that vessels $<20\mu\text{m}$ will be affected by aliasing. Indeed, in the context of window-chamber imaging, Vakoc et al demonstrated good correlation between multiphoton microscopy and OCT angiograms (Using a mean lateral spacing of $\sim 6.3 \mu\text{m}$) for large vessels, however capillaries which were below 12 μm in diameter exhibited poor correlation due to them appearing wider with OCT[7]. Given the qualitatively thinner vessel morphologies visible within the fs188 tumors (fig. 4) it is likely that this spatial dilation has a larger effect on the mean fs188 vessel diameters than the corresponding fs120 measurements. However, the differences between tumor types remain significant.

The total vessel length per mm^2 (mm/mm^2) was significantly higher for the fs120 tumors ($4.3 \pm 1.5 \text{ mm}^{-1}$) than the fs188s ($2.2 \pm 0.7 \text{ mm}^{-1}$). Similarly, a higher overall vessel density was measured in the fs120 tumors ($31.7 \pm 11.1\%$) compared to the fs188 tumors ($14.8 \pm 5.0\%$). These observations agree with density calculations performed by CD31 stained vessel counting[30]. Interestingly, window-chamber observations yielded a lower total vessel length per mm^2 for fs120 tumors, the opposite to what is observed here[16]. Its highly likely that such discrepancies result from the different depths / quantification methods of the tumor circulation under consideration. Indeed, the reduced infiltration of the fs188 tumor vasculature to the more superficial layers of skin, as observed in sections 3.1 and 3.3, would directly result in lower lengths of overall detected fs188 vasculature, particularly since skeletonization was performed on projections over a large 0-800 μm depth range. It would be useful to compare the observed length per mm^2 at equivalent depths within the tissue. However, a direct comparison between vessel lengths at the green depth of fig. 4 (400-800 μm) would yield inaccurate results for the fs120 tumors because much of the green vasculature is directly occluded due to the shadowing artefact cast downwards from the more superficial red vasculature[7]. An alternative is to perform the measurement over a smaller depth “window”, e.g. by considering only the first 100 μm of visible vasculature, decoupled from its axial position within the tissue. To investigate this, mean-intensity-projection images were captured over a 100 μm depth with the superficial layer of the projection window placed where the first tumor vasculature was visible. When processed in this manner, the fs120 tumors displayed significantly ($p=0.04$) lower vessel length per mm^2 ($1.5 \pm 0.7 \text{ mm}^{-1}$) compared to fs188 tumors ($2.2 \pm 0.3 \text{ mm}^{-1}$). However, it remains unclear if depth dependent metrics such as total vascular length / density are reliable when compared at different depths within the tissue.

No significant difference in the mean vessel segment length between the tumor types was observed, in agreement with the previous window-chamber observations[16]. Both the mean tortuosity and the fractal dimension of the vessel networks were found to be significantly higher for the fs120s (1.56 ± 0.29 and 1.33 ± 0.17 respectively) compared to the fs188s (1.33 ± 0.13 and 0.98 ± 0.18 respectively). Given that there was no difference in the mean vessel segment length between the tumor types, a higher tortuosity for the fs120 tumors must mean that the branch points of the fs120 network are closer together than those of the fs188 tumors but the vessels themselves are more tortuous between the branchpoints. This is reflected in the fractal dimension measurements, with the lower value of fractal dimension for fs188s being indicative of a more regular, organized vessel network. This is again consistent with the previous observations of these tumor types with intravital microscopy, with fs120 vessels being described as generally wider and very chaotic in their arrangement, while fs188 vessels are described as regularly organized and uniformly narrow[16].

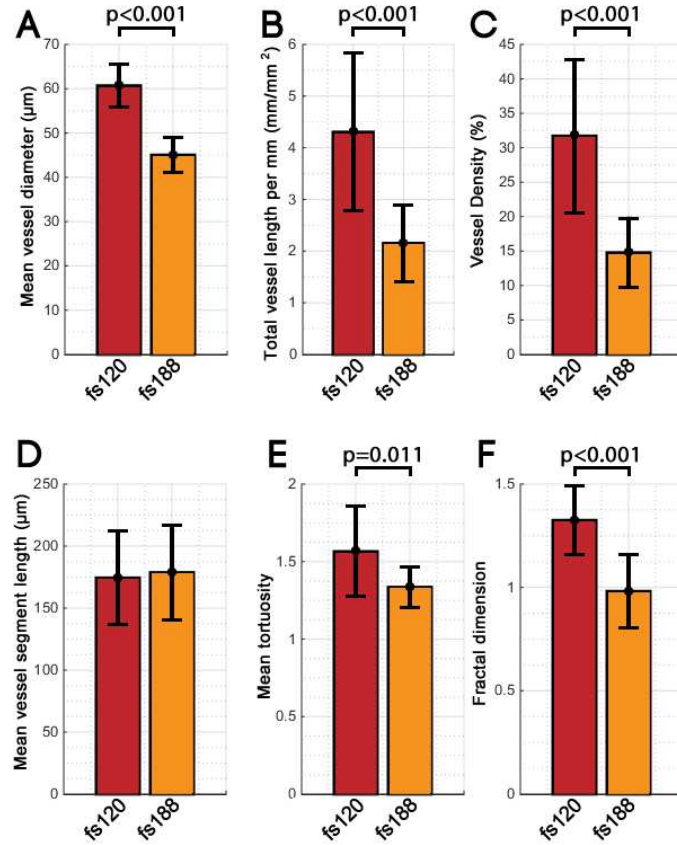


Fig. 10 – The variation in quantitative vessel parameters between fs120 tumors (n=9) and fs188 tumors (n=8) at the study endpoint. Columns: The average value of each respective quantitative parameter across the entire fs120 or fs188 group. (bars, standard deviation). Statistical significance calculated using an independent two-sample t-test between the fs120 and fs188 datasets.

4. Conclusions

OCT is able to non-invasively quantify morphological differences in the superficial vasculature of subcutaneously implanted murine tumors expressing different VEGF isoforms, providing results that are consistent with those acquired by more conventional methods in previous studies[16]. OCT does not require the use of a transparent optical window and allows tumors to grow and be observed in a three-dimensional environment. Bulk-tissue-motion artefacts resulting from breathing or other muscular movements are effectively suppressed through a combination of in-plane registration, correlation optimization and combined wavelet-FFT filtering. Longitudinal tumor monitoring is achievable, with a high degree of vessel co-registration between scans. However rapid variations in day-to-day vascular density are present, which may arise from the use of general anesthesia. This limitation could potentially be addressed in future through utilization of a high-speed OCT system, which may negate the requirements for anesthesia and physical pressure to reduce movement. This would make it feasible to longitudinally quantify the effects of angiogenic inhibitors or other treatments that directly affect the vasculature within solid tumors.

Tumors that solely express the VEGF120 isoform were more invasive, penetrating to more superficial levels of the skin than the VEGF188 variants. Thinning of the hypodermis in the skin encapsulating both types of solid tumor leads to an improved depth penetration compared to healthy skin. Furthermore, disruption of the striated muscle (*panniculus carnosus*) layer was particularly common for the VEGF120 expressing tumors. Morphologically, the fs120 vessels appeared wider and formed dense, more disorganized networks when compared to the fs188 vessels, which tended to form thinner more organized networks. This is evidenced by a significantly higher mean vessel diameter, length, tortuosity and fractal dimension for fs120 tumors.

The successful differentiation between these tumor types with OCT suggests that the known morphological differences in tumor vascularity persist outside of the window chamber model and are measurable without surgical intervention. Furthermore, the wound healing response to surgical intervention involves release of angiogenic factors such as angiopoietin-2 (Ang-2) from endothelial cells[31], which can compromise the use of the window chamber model in studies of putative anti-angiogenic therapeutics[32]. OCT has the necessary spatial resolution to provide an alternative and non-invasive method to quantify the vascular response of superficial tumors to such therapy.

Funding

This research was supported by BBSRC Doctoral Training Grant: BB/F016840/1. The authors also gratefully acknowledge the use of equipment funded by MRC grant: MR/L012669/1.

Disclosures

The authors declare that there are no conflicts of interest related to this article.